

---

# VIRTUAL HYPERSPECTRAL IMAGES USING SYMMETRIC AUTOENCODERS

---

A PREPRINT

Archisman Bhattacharjee<sup>1</sup>, Pawan Bharadwaj<sup>2</sup>, and Laurent Demanet<sup>3</sup>

<sup>1,2</sup>Center for Earth Sciences, Indian Institute of Science, Bengaluru, India

<sup>3</sup>Dept. of Mathematics and Earth Resources Laboratory, Massachusetts Institute of Technology, Cambridge, USA

September 26, 2023

## ABSTRACT

Spectral data acquired through remote sensing are invaluable for environmental and resource studies. However, these datasets are often marred by nuisance phenomena such as atmospheric interference and other complexities, which pose significant challenges for accurate analysis. We show that an autoencoder architecture, called SymAE, which leverages symmetry under reordering the pixels, can learn to disentangle the influence of these nuisance from surface reflectance features on a pixel-by-pixel basis. This disentanglement provides an alternative to atmospheric correction, without relying on radiative transfer modeling, through a purely data-driven process. More importantly, the symmetric autoencoder can generate virtual hyperspectral images by manipulating the nuisance effects of each pixel. We demonstrate using AVIRIS instrument data that these virtual images are valuable for subsequent image analysis tasks. We also show SymAE’s ability to extract intra-class invariant features, which is very useful in clustering and classification tasks, delivering state-of-the-art classification performance for a purely spectral method.

## Keywords

autoencoders, atmospheric corrections, hyperspectral imaging, nuisances, redatuming, virtual images, hyperspectral image classification

## 1 Introduction

Complications due to nuisance or uninteresting parameters arise in many inverse problems. In remote sensing of the Earth’s surface, nuisance effects could be associated with atmospheric effects, sensor noise, sun-angle variations, topographic effects, spatial intra-class variations, spectral mixing, and instrumental and data artifacts [1, 2]. The presence of such nuisance can make the inference of useful surface reflectance features highly uncertain.

Therefore, dealing with these nuisance effects is seen as a critical pre-processing step. In this note, we demonstrate the utility of an autoencoder [3, 4] architecture, called the symmetric autoencoder [5, SymAE], to *uniformize* the nuisance effects in hyperspectral images. To illustrate this, envisage a collection of pixels belonging to a specific class. Among these, certain pixels might be obscured by cloud cover, while others enjoy the clarity of an unobstructed sky. Through SymAE’s process of *redatuming*, nuisances can be transposed from one pixel to another, effectively generating virtual pixel spectra. These synthesized pixels can be systematically manipulated to simulate either cloudless or cloudy conditions — effectively aligning pixels in terms of their nuisance effects as shown in Figure 1.

Our approach holds significant potential for applications such as mineral characterization, land cover identification, and hyperspectral signature analysis. It becomes especially valuable when dealing with classes exhibiting subtle differences that are muddled by the variance introduced by nuisance effects. Ultimately, our experiments demonstrate that

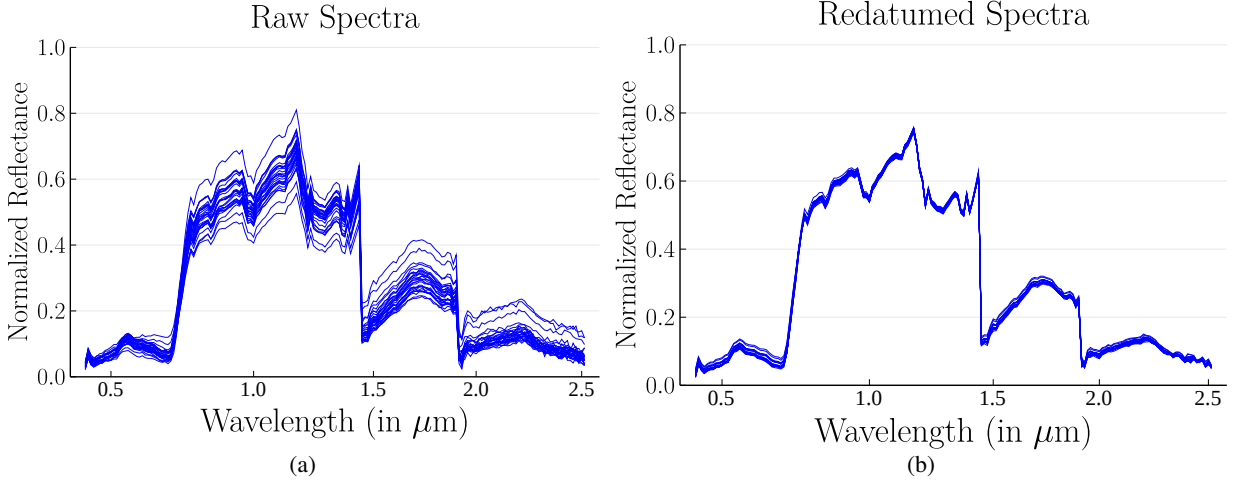


Figure 1: Example from the Kennedy Space Center dataset. (a) Original spectra in the dataset belonging to Oak Hammock vegetation class. These pixel spectra showcase dissimilarities possibly arising from nuisance effects like atmospheric or ground-based variations. (b) The raw spectra undergo the redatuming process to generate virtual spectra, as depicted here. Through redatuming, the spectra share nuisance effects, leading to uniformity among spectra while preserving vegetation-class-specific reflectance features. In the subsequent examples presented in this paper, we employ band indices to annotate the x-axis of the spectra, consistent with standard remote sensing datasets where the wavelength of radiation is well understood.

employing this architecture enables us to achieve hyperspectral image (HSI) classification performance comparable to that of other state-of-the-art networks and outperforming them for a purely spectral method.

SymAE constitutes an encoder that provides a compressed latent representation of the input hyperspectral image on a pixel-by-pixel basis and a decoder that reconstructs the input in a near-lossless manner. The latent representation of this autoencoder is valuable because each at-sensor pixel spectrum is decomposed into two components (dimensions): one correlated to nuisance parameters and another to the surface reflectance features. Specifically, a disentangled representation can be used to manipulate the nuisance information of the pixels, e.g., the swapping of the atmospheric effects of a given pixel with another. As will be discussed later, swapping nuisance effects is equivalent to decoding a hybrid latent code prepared by mixing components of the latent code between the respective pixels. Consequently, the atmospheric effects can be uniformized across the pixels, producing a new virtual hyperspectral image. It should be crucially emphasized that the SymAE executes the aforementioned decomposition in a model-free manner, excluding the need for atmospheric radiation transfer models that typically demand prior information about nuisance parameters — examples being aerosols, gases, clouds, and water vapor distribution. Virtual hyperspectral images can be of several uses:

- as redatuming can be seen as an alternative to atmospheric correction, virtual images can be useful in environments where physical models of the atmosphere have high uncertainties;
- better image processing tasks such as classification, segmentation, etc. can be performed on virtual images with uniformized nuisance effects;
- virtual hyperspectral images enable scenario analysis, i.e., simulating the spectra under different atmospheric or nuisance conditions enabling more accurate surface characterization.

Traditional autoencoding ideas alone will not guarantee that the surface reflectance features and nuisance features of an input spectrum are encoded as separate components in the latent space. To accomplish data-driven representation learning, we harness the property of permutation invariance found in surface reflectance of pixels with common features. In other words, when examining a group or a cluster of pixels within extensive remote-sensing datasets, possessing identical surface-reflectance information — this information remains unaffected by the arrangement or the ordering of pixels within this group. Specifically, we capitalize on grouping the observed spectra a priori to structure the latent space. The identification of these groups is application-specific, and some ideas are discussed in Section 2. Finally, the latent representation of the SymAE is guided by specific constraints linked to these grouped spectra, encompassing:

- Firstly, the surface-reflectance characteristics within a particular group exhibit symmetry concerning the arrangement of its spectra. In essence, the surface reflection information is assumed to be coherently shared across the spectra within the group.
- Secondly, the nuisances across the spectra within a given group are distinct, i.e., each spectrum experiences a distinct unwanted alteration, influenced by corresponding nuisance phenomena. For example, we assume that the pixels within a group contain effects due to diverse atmospheric configurations.

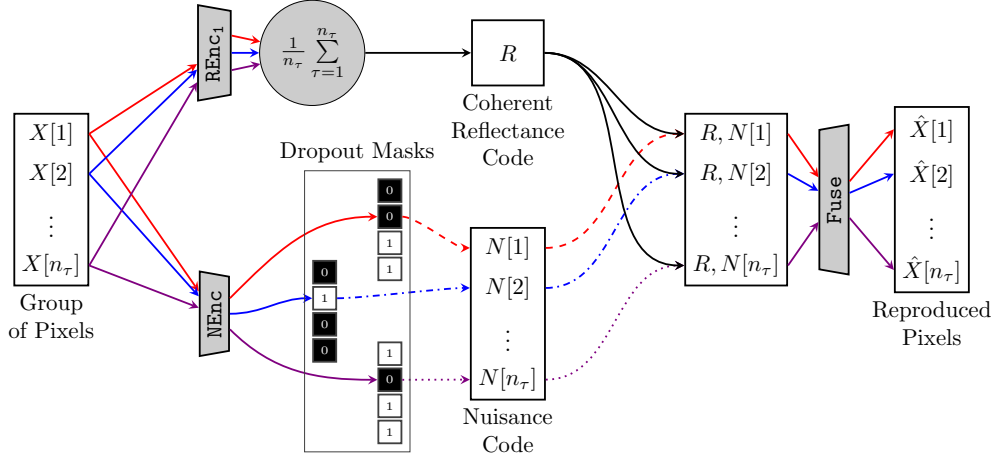


Figure 2: The architecture of a symmetric autoencoder disentangles surface reflectance information from the nuisance (for example, atmospheric scattering) effects in its latent space. The surface-reflectance information is assumed to be coherent across the pixels in a group. Therefore, it can only propagate through the network via solid arrows — notice that the dropout masks prevent its propagation. Colored arrows to indicate the propagation of the remaining nuisance effects — notice that a symmetric function, i.e., symmetric w.r.t. the ordering of pixels, prevents its propagation.

These constraints collectively steer SymAE’s learning process, facilitating the creation of a latent representation that captures the essential features while accounting for the complexities introduced by nuisances. SymAE training is a highly generalized form of blind deconvolution that uses the merging of different latent variables in a neural network to replace the notion of convolution. The architectural design choices of SymAE, which are made to ensure that the constraints mentioned above are satisfied, are detailed in [5].

Before we delve further, we wish to underscore the nuanced nature of the term *surface-reflectance*, which we will consistently employ throughout the remainder of this article. Although we assert our intention to disentangle these features from the spectra, we are, in fact, more accurately extracting *coherent features* from within spectral groups. To illustrate this, consider a collection of spectra obtained through multiscan hyperspectral imaging of a specific location at various instances, each affected by diverse atmospheric conditions. In this context, the repeated measurement of reflectance from identical surface constituents ensures that surface information remains coherent across pixels. It is worth noting here that while the term ‘coherent features’ might seemingly overlap with surface-reflectance features, certain atmospheric attributes could exhibit coherency across multiscan measurements. Additionally, surface reflectance might undergo seasonal changes, e.g., due to variations in surface moisture content, etc. However, due to the inherent challenge of physically labeling the coherent information and the fluidity of coherency based on the application context, we will frequently use the term ‘surface reflectance’ when discussing concepts in this paper. It is crucial to recognize that within the framework of the Symmetric Autoencoder (SymAE), the classification of information into coherent information and nuisance information depends on the strategies used for grouping. This paper highlights the advantages of disentangling the coherent information through spectral grouping for classification and surface characterization tasks, in contrast to working with the raw spectra.

Image processing for eliminating the atmospheric effects from hyperspectral images is tedious in a setting with lack of prior information about the atmosphere. We provide an alternative to traditional atmospheric corrections, avoiding the need for complex radiative transfer modeling and instead use a purely data-driven approach. SymAE does not rely on the atmospheric prior, as opposed to radiative transfer approaches [6, 7, ?] that can simulate the absorption and scattering effects of atmospheric gases and aerosols to correct the hyperspectral images. Several scene-based empirical approaches are developed for atmospheric correction [9, 10]. These approaches do not rely on radiative transfer modeling of the atmosphere. However, the applicability of these approaches is limited due to unrealistic requirements, e.g., the flat-field correction [11] approach requires the availability of an area in the scene that has flat reflectance

spectra; The empirical-line approach [12] requires field-measured spectra to derive atmospheric corrections. Our approach belongs to this class of scene-based approaches since SymAE is trained to automatically learn the nuisance characteristics while processing large volumes of the observed data. However, more importantly, we believe that our requirement of grouping the observed spectra is less restrictive and therefore more practical.

Deep learning algorithms are popular for remote-sensing image analysis tasks such as image fusion, registration, scene classification, semantic segmentation, and pixel-based classification [?]. Like SymAE, some contemporary architectures [14, 15] offer a fundamentally different way of correcting the atmospheric effects in images. The authors of [15] use synthetic spectra from radiative transfer modeling to train an atmospheric-correction network in a supervised setting — our data-driven approach does not involve radiative transfer modeling. Furthermore, the permutation invariance property used in the architecture of SymAE enables it to extract features common to specific classes which make classification tasks easier. Permutation invariance has been previously used in the context of remote sensing in [16] for multiscan data to obtain super-resolution of images. While generative models like Generative Adversarial Networks (GANs) have found application in remote sensing [17, 18], our approach offers a distinctive interpretational advantage. It enables the differentiation of nuisance features from class-specific surface reflectance features within latent codes. The interpretability of these features depends on the prior grouping step, which holds the potential of enhancing our understanding of the data, setting our approach apart from conventional generative models.

## 2 Spectral Grouping

Our approach necessitates a priori grouping of spectra to effectively disentangle nuisance effects. All the spectra in a given group are presumed to contain identical coherent information but dissimilar nuisance effects. The number of such identifiable groups is the application and scene-specific. If we intend to disentangle atmospheric and lighting variations from surface reflectance, an ideal scenario for achieving this objective is one in which multi-scan hyperspectral data is available. In this setup, each pixel undergoes multiple scans under diverse atmospheric conditions and varying elevation angles. Here, each group of spectra pertains to the same pixel but exhibits varying atmospheric influences. In this context, SymAE proves invaluable for disentangling atmospheric nuisances and pixel-specific reflectance in an entirely unsupervised manner.

Acknowledging the challenges in acquiring multi-scan data for real-world applications, we concentrate instead on single hyperspectral scenes. The grouping task is straightforward if distinct spatial features (e.g., water bodies, crops, asphalt, etc.) are identifiable in the image. In addition, pixels that are classified with high certainty during a preliminary analysis can also assist the grouping task. Specifically, our approach in this paper involves grouping pixels using a priori information derived from two sources: 1) ground truth labeling and 2) spatial proximity. Leveraging ground truth information entails forming groups based on assigned pixel classes, such as specific vegetation or land types, in hyperspectral images. Note that the variations in textures, spectral mixing, and other atmospheric factors exist even among pixels of the same class, contributing to what we refer to as nuisance effects. During training, we utilized approximately 10% of the ground truth information. We showcase its performance on the remaining test pixels of the scene in Section 4. In cases where ground truth labels are limited, we adopt an alternative approach by working with groups of spatially proximate pixels (groups of 9 pixels, present in  $3 \times 3$  patches). Here, SymAE is trained to extract spatially-coherent features. Although we acknowledge that this spatial grouping method is less efficient than using ground truth, we analyze its advantages in Section 5.

A hyperspectral image is inherently three-dimensional, with the first two dimensions representing the spatial domain, and the third dimension corresponding to the spectral domain. To facilitate our analysis, we group pixels into distinct sets, bundling together all pixels belonging to the same group. These grouped pixels are utilized for training our autoencoder after constructing a set of datapoints denoted as  $\{X_i\}_{i=1, \dots, n_X}$ . Each datapoint,  $X_i$ , comprises a selection of pixels randomly drawn, with replacement, from the same group. The datapoints are assigned to all the available groups uniformly. In our notation,  $[A; B]$  signifies the vertical concatenation of two vectors,  $A$  and  $B$ . To access individual pixels within a datapoint, we index them as  $X_i[\tau]$ , where  $\tau$  ranges from 1 to  $n_\tau$ . Consequently,  $X_i$  is constructed as  $[X_i[1]; \dots; X_i[n_\tau]]$ . Each pixel spectrum, represented by  $X_i[\tau]$ , is a vector of length equal to the number of frequency bands. These constructed data points serve as the basis for training SymAE, with further details provided in the subsequent section.

## 3 Symmetric Autoencoder

We constructed the datapoints such that the surface reflectance is *coherent* across the pixels of each datapoint. The goal of symmetric autoencoder [5] to disentangle this coherent reflectance information from the remaining nuisance variations, e.g., atmospheric effects, in its latent space. Autoencoders [19] are comprised of two components: an

encoder  $\text{Enc}$  that maps each datapoint  $X_i$  into latent code  $H_i = \text{Enc}(X_i)$ , and a decoder  $\text{Dec}$  that attempts reconstruct to  $X_i$  from the code. We determine both the functions  $\text{Enc}$  and  $\text{Dec}$  by minimizing the reconstruction loss

$$\text{Enc}, \text{Dec} = \arg \min_{\text{Enc}, \text{Dec}} \sum_i \|X_i - \text{Dec}(\text{Enc}(X_i))\|^2 \quad (1)$$

over the training datapoints. SymAE relies on a unique encoder architecture, as depicted in Figure 2, to structure the latent space. This architecture can be mathematically described by

$$\text{Enc}(X_i) = [\text{REnc}(X_i); \text{NEnc}(X_i[1]); \dots; \text{NEnc}(X_i[n_\tau])]. \quad (2)$$

As a result, the latent code  $H_i = [R_i; N_i[1]; \dots; N_i[n_\tau]]$  is partitioned into the following interpretable components of each datapoint  $X_i = [X_i[1]; \dots; X_i[n_\tau]]$ :

1. the component  $R_i = \text{REnc}(X_i)$  contains the surface-reflectance information as it is coherent across the pixels of  $X_i$
2. the remaining components  $N_i[\tau] = \text{NEnc}(X_i[\tau])$  complement  $R_i$  with pixel-specific nuisance information.

Finally, SymAE’s decoder  $\text{Fuse}$  non-linearly combines code  $R_i$  with each pixel-specific code  $N_i[\cdot]$  to reconstruct the original datapoint pixel-by-pixel

$$\begin{aligned} \hat{X}_i &= \text{Dec}(H_i) = \text{Dec}([R_i; N_i[1]; \dots; N_i[n_\tau]]) \\ &= [\text{Fuse}([R_i; N_i[1]]); \dots; \text{Fuse}([R_i; N_i[n_\tau]])]. \end{aligned}$$

Here, no constraints are enforced on functions  $\text{NEnc}$  and  $\text{Fuse}$  as they are parametrized using fully-connected layers. On the other hand, to ensure  $\text{REnc}$ , the *reflectance encoder*, only encodes the coherent reflectance, we constrain it to be invariant under permutations of the pixels in  $X_i$ . In other words, for all permutations  $\Pi$  along the pixel dimension, we desire that

$$R_i = \text{REnc}(X_i) = \text{REnc}(X_i[\Pi(1:n_\tau)]) \quad (3)$$

purely represents the coherent information since  $R_i$  does not depend on the labeling of the pixels in  $X_i$ . Moreover, it is important to note that the nuisance effects, which are dissimilar across the pixels, cannot be encoded using  $\text{REnc}$  without significant loss of information.

SymAE’s reflectance encoder explicitly achieves the invariance mentioned above using a permutation-invariant network architectures following [20] which provide universal approximation guarantees for symmetric functions. These architectures use pooling functions such as the mean or the max across the instances to ensure permutation invariance. In our experiments, the spectrum of each pixel is simply transformed using  $\text{REnc}_1$ , an unconstrained function parametrized using fully-connected layers, and mean taken along the pixel dimension

$$R_i = \left( \frac{1}{n_\tau} \sum_{\tau=1}^{n_\tau} \text{REnc}_1(X_i[\tau]) \right). \quad (4)$$

We emphasize that the key observation in this equation is that the mean of the *transformed instances*  $\text{REnc}_1(X_i[\tau])$  is symmetric with respect to the ordering of pixels. This ensures that the desired symmetry (eq. 3) is achieved. SymAE’s nuisance encoder  $\text{NEnc}$  is unconstrained. This aspect is a significant concern as the decoder  $\text{Fuse}$  might tend to ignore the  $R_i$  component in favor of using purely  $N_i[\cdot]$  information for reconstruction.

As the purpose of  $\text{NEnc}$  is exclusively to encode pixel-specific nuisance information while disregarding surface reflectance, SymAE incorporates *dropout masks* during training via Bernoulli dropout [21] with a probability of  $p = 0.5$ :

$$N_i[\tau] = \text{Dropout}(\text{NEnc}(X_i[\tau])). \quad (5)$$

The dropout introduces random obfuscation to elements of  $N_i$ , making the decoder  $\text{Fuse}$  perceive the codes as dissimilar and hindering the reconstruction of coherent surface-reflectance information from  $N_i$ . While there is a continuous stream of information from  $\text{REnc}$ , the outputs of  $\text{NEnc}$  intentionally introduce noise, with certain features being randomly obfuscated. This compels  $\text{Fuse}$  to extract as much meaningful information as possible from  $R_i$ , which inherently contains coherent data. Over time,  $\text{Fuse}$  becomes adept at capturing all coherent information from  $\text{REnc}$ , with the remaining pixel features learned from  $N_i$  encoded by  $\text{NEnc}$ . At test-time, the entirety of the  $N_i$  code is sent unaltered into the decoder. Finally, the functions  $\text{NEnc}$ ,  $\text{REnc}_1$  and  $\text{Fuse}$  are trained concurrently by minimizing Eq. 1 with the dropout mechanism just described. The success of SymAE requires a sufficiently large number of pixels with *dissimilar* nuisance variations in each group to achieve the desired structure of the latent space.

### 3.1 Virtual Hyperspectral Images

Using a trained SymAE network, we can generate a virtual hyperspectral image by redatuming each of the measured pixel spectra. The redatuming is performed pixel-by-pixel by swapping the nuisance effects in a given spectrum with a reference pixel. Redatuming data is equivalent to manipulations in the latent space. Precisely, to redatum the  $k$ th pixel spectrum  $D[k]$ , we first extract its reflectance code using  $\text{REnc}_1(D[k])$ . We then fuse this code with the nuisance code of the reference spectrum (indexed using  $k_0$ ) to obtain a virtual spectrum

$$\hat{D}_{k_0}[k] = \text{Fuse}([\text{REnc}_1(D[k]); \text{NEnc}(D[k_0])]), \quad (6)$$

which is not originally measured. Therefore, SymAE allows for *scanning* the area corresponding to pixel  $k$  with nuisance conditions present during the observation of pixel  $k_0$ . The virtual image  $\hat{D}_{k_0}$  is generated by collecting all the virtual spectra with similar nuisance effects.

## 4 Training With Ground Truth

In this section, we perform spectral grouping using ground truth information to showcase the application of SymAE. We utilize a hyperspectral image acquired by NASA’s AVIRIS instrument over the Kennedy Space Center (KSC), Florida, on March 23, 1996. The image has dimensions of  $512 \times 614$  pixels and comprises 176 spectral bands. While this dataset was corrected using the ATREM [22, Atmosphere Removal Program] method based on radiative transfer modeling, researchers [23] have highlighted the necessity for post-ATREM polishing due to errors in solar irradiance models and atmospheric parameter estimations. The differences in spectral signatures among certain vegetation types may appear subtle. However, due to the presence of nuisance effects, these spectral signatures can exhibit notable discrepancies, even within pixels belonging to the same class. Consequently, the correction of residual nuisance effects, referred to as *polishing*, becomes imperative to ensure accurate discrimination of land cover in this environment.

To train SymAE, we partitioned the ground truth data into separate test and training sets. As mentioned earlier, our training set comprised approximately 10% of pixels from each class provided as ground truth within the dataset. Subsequently, we organized the training set pixels into groups corresponding to the ground truth categories. Our training process involved  $n_X = 524288$  data points, utilizing  $n_\tau = 8$  and a mini batch size of 256. The dimensions of the latent codes,  $R_i$  and  $N_i$ , were both set to 64. For further details regarding the configuration of the architecture, a Jupyter notebook written in Julia using the Flux package [24] is shared on <https://github.com/archieb1999/SymAE.KSC>.

After completing training, we generated virtual spectra using Equation 6 with randomly selected reference pixels. The resulting vegetation spectra exhibited a notably reduced intra-class variance, suggesting the uniformization of nuisance effects across these spectra. This is visually demonstrated in Figure 3, where the spectra display a significant decrease in intra-class variance after undergoing the redatuming process. The autoencoder not only exhibits a high degree of proficiency in redatuming within the training set, but the variance is also considerably reduced in the case of test ground truth pixels that were excluded during training. Furthermore, it is noteworthy that subtle inter-class differences are retained throughout the redatuming process. These findings underscore the motivation for utilizing the redatumed pixels in subsequent classification and characterization tasks.

To quantify the extent of nuisance effects among pixels within a specific ground truth class, we employ the metric of *average variance*. Initially, we calculate the variance in spectral reflectance for each band, followed by computing the average of these variance values. This average effectively represents the overall variance among all spectra belonging to a particular ground truth class. A higher average variance indicates that the pixels within the chosen class exhibit significant dissimilarities. Post-redatuming, we anticipate observing a reduction in variance. This reduction is apparent in Table 1, which presents the average variance values both before and after redatuming with a random pixel. Notably, following the redatuming procedure, the residual average variance in the test pixels is consistently below 5% for the majority of the classes.

However, we wish to emphasize that the choice of a reference pixel can significantly impact virtual spectra. In our methodology of a priori grouping, which relies on ground truth data, we have observed that nuisance features are not limited to atmospheric and lighting effects; they could also include ground-based factors. These factors encompass spectral mixing, surface moisture content, and texture, among others, and they may add complexity to the virtual spectral analysis. It is noteworthy that these nuisance effects may affect different classes to varying degrees. For instance, marsh classes may be more susceptible to spectral variations due to surface water content than upland vegetation classes, potentially resulting in substantial fluctuations in energy reflected from marsh pixels. Additionally, some nuisance phenomena may pertain to specific classes but might not exist for others. For example, features related to crop ripeness may not be relevant in the context of water bodies. Thus, the degree of correspondence between generated virtual images and real-world scenarios may depend on the choice of reference pixel. Therefore, if the intention is to

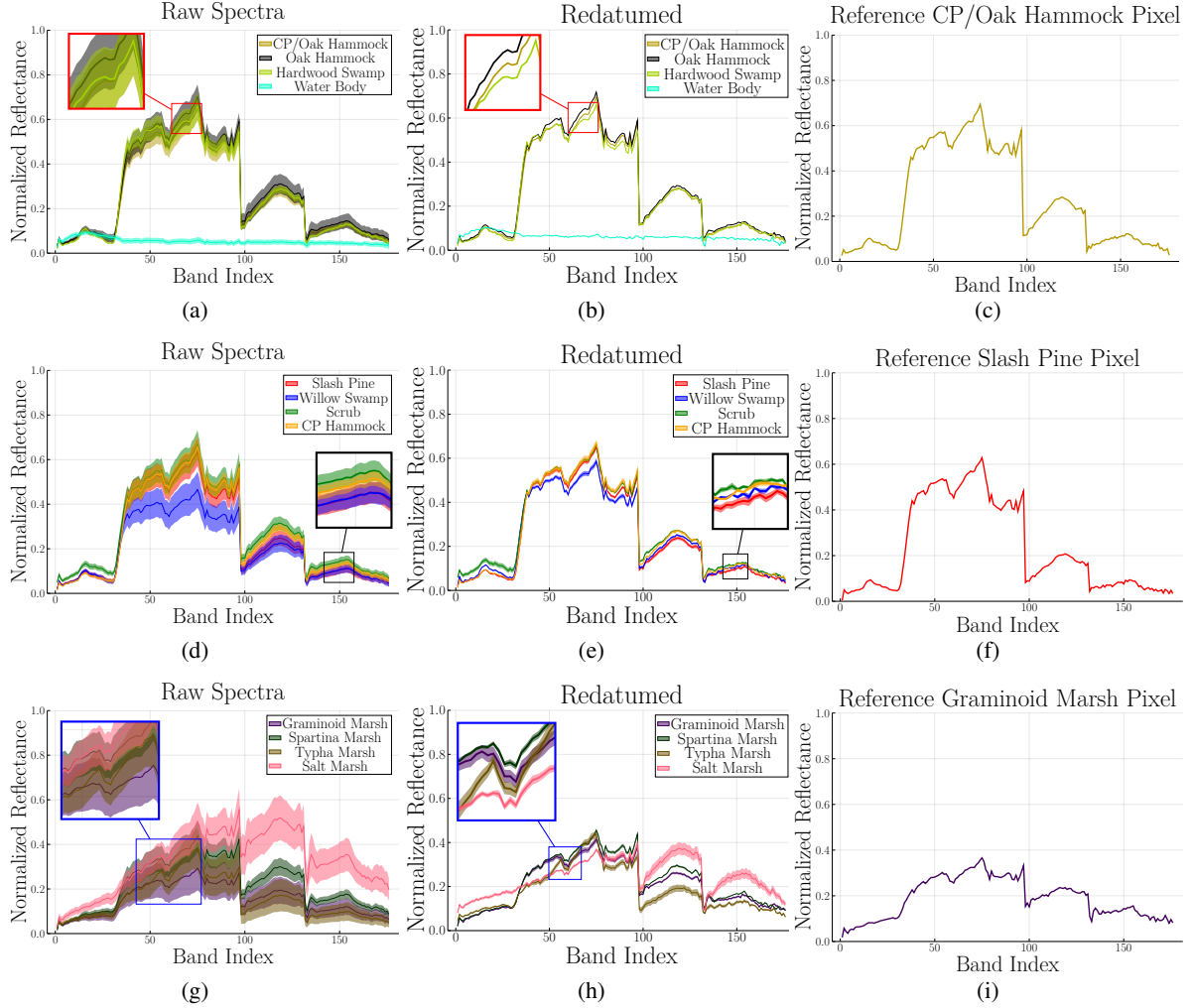


Figure 3: Ribbon plots illustrate reduction in intra-class variance post-redatuming. Each ribbon plot represents spectral distribution of distinct classes, with central line denoting mean and ribbon’s width on either side indicating intra-class standard deviation. (a) Displays train set spectra from four distinct classes, while (b) shows their respective redatumed counterparts, wherein pixels from the same classes almost coincide, and (c) shows the reference pixel used for redatuming. (d)-(f) Show spectra from test set upland vegetation classes, following the pattern observed in (a)-(c). While not as pronounced as in (b), the redatumed test set pixels exhibit a discernible reduction in intra-class variance. (g)-(i) are same as (d)-(f) but for wetland classes.

Table 1: Effective redatuming leads to a reduction in the average variance among the testing pixels corresponding to different ground truth classes within the KSC dataset.

No.	Class	Training Samples	Test Samples	Average Variance In Raw Spectra ( $\times 10^{-6}$ )	Average Variance After Redatuming ( $\times 10^{-6}$ )	Residual Variance (%) After Redatuming
1	Scrub	77	684	1173.9	24.6	2.10 %
2	Willow Swamp	25	216	1938.3	17.0	0.88 %
3	CP Hammock	26	230	591.9	38.0	6.42 %
4	CP/Oak Hammock	26	225	1267.6	43.5	3.43 %
5	Slash Pine	17	144	1315.4	22.2	1.69 %
6	Oak Hammock	23	206	1346.5	61.5	4.57 %
7	Hardwood Swamp	11	94	695.3	9.4	1.35 %
8	Graminoid Marsh	44	387	3466.7	51.0	1.47 %
9	Spartina Marsh	52	468	1530.9	132.3	8.64 %
10	Typha Marsh	38	339	3086.0	141.1	4.57 %
11	Salt Marsh	42	377	3986.9	415.4	10.42 %
12	Mud Flats	47	415	1529.5	325.1	21.26 %
13	Water Body	91	817	143.0	0.047	0.03 %



employ redatuming for detailed spectral and scenario analysis, we suggest selecting reference pixels with relatively similar nuisance feature distributions if prior information is available. Apart from a small example in the upcoming subsection, a detailed study on the interpretability of virtual spectra is beyond the scope of this paper. Instead, our primary focus in this paper is on the advantages of uniformizing nuisance features across spectra and extracting spectral features to enhance clustering and classification performance.

#### 4.1 Comparison to Denoising Autoencoders

Denoising Autoencoders (DAEs) represent a class of neural networks frequently employed in unsupervised learning. They are recognized for their proficiency in recovering underlying data representations by intentionally introducing noise into input data [25]. In the field of remote sensing and hyperspectral image (HSI) analysis, various iterations of Denoising Autoencoders (DAEs) have been applied in previous studies [26]. In this study, we sought to compare the noise reduction achieved by denoising autoencoders with that of SymAE. Our observations indicate that while denoising autoencoders tend to smooth the spectral data, they fall short of significantly mitigating intra-class variance, as depicted in Figure 4b. DAEs typically assume a noise distribution, such as Gaussian, for denoising spectra. In

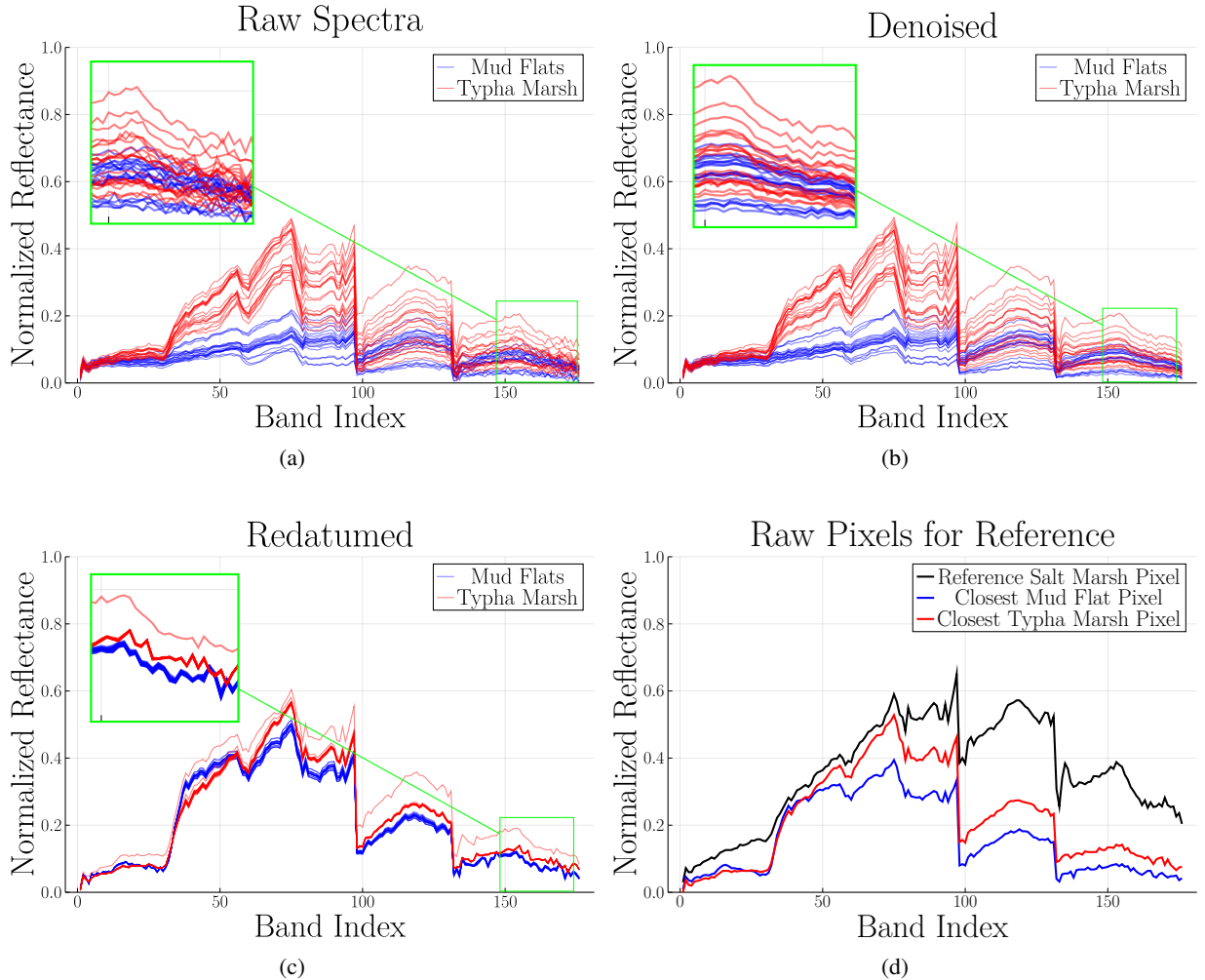


Figure 4: Comparative analysis of application of DAE and SymAE on test data. (a) Raw spectra from two land-cover classes in Kennedy Space Center scene. (b) DAE demonstrates a propensity to smooth spectral data, yet notable within-group variations remain evident. (c) Redatuming, as implemented by SymAE, outperforms denoising by DAE in mitigating intra-class variance. However, it is important to note that redatumed spectra may exhibit significant dissimilarities from the original raw spectra. (d) Shows the reference Salt Marsh pixel used for the redatuming, along with pixels from the respective ground truth classes that are closest to the redatumed spectra.



contrast, SymAE adopts a different approach, learning the distribution of the underlying nuisance/noise after spectral grouping. Remarkably, utilizing SymAE resulted in a noticeable reduction in intra-class variance, highlighting its efficacy in capturing and discerning the distinctive features among different classes.

As mentioned earlier, it is important to recognize that the virtual spectra are contingent upon the reference pixel chosen during the redatuming process. While our demonstrations illustrate that a task such as classification remains relatively unaffected by the choice of this reference pixel, interpreting the virtual spectra may not be straightforward. These spectra are still influenced by the residual nuisance features present in the reference pixel. To illustrate this, we intentionally selected a Salt Marsh pixel with relatively high reflected energy (as shown in Figure 4d) for redatuming Mud Flats and Typha Marsh pixels, as depicted in Figure 4c. Post-redatuming, the virtual spectra manifest noticeably elevated energy levels compared to their raw counterparts. This phenomenon likely stems from our autoencoder’s incorporation of overall reflected energy as an element within the nuisance features. Nevertheless, the redatumed spectra still maintain a shape resembling the pixels closest to them in their respective ground truth classes, as referenced in subfigure 4d.

In essence, the SymAE-generated virtual images are not completely *denoised*; they still retain residual nuisance effects originating from the reference pixels. Nonetheless, due to the uniformity of nuisance features across the entire image, the relative distinctions among redatumed pixels can prove invaluable for subsequent image-processing tasks.

## 4.2 Virtual Images: Classification

SymAE introduces a valuable capability to visualize hyperspectral image locations under varying virtual conditions, which has the potential to enhance pixel classification accuracy and extend the possibilities of hyperspectral image analysis. To exemplify the benefits brought about by redatuming and the uniformization of nuisance effects across pixels, we conducted K-Nearest Neighbor (KNN) classification, with  $K = 5$ , on both the raw and virtual hyperspectral images. These results are presented in Figure 5. For the raw image, the overall accuracy for the test pixels aligned with the ground truth stands at 81.6%, a lower figure primarily attributed to the presence of nuisance effects. However, when applied to the virtual images after the uniformization of nuisances, the overall accuracy elevates significantly to  $92.8 \pm 0.9\%$ . In a parallel approach, we assessed the performance of two classical machine learning models on our test set: 1) Random Forests and 2) linear Support Vector Machines (SVM). The outcomes distinctly underscore the significance of SymAE-generated virtual images: an evident enhancement in predictive overall accuracy (OA) for both Random Forests (e.g., 86.2% accuracy for raw images versus a noteworthy  $93.0 \pm 0.9\%$  overall accuracy for virtual image) and linear SVM classifiers (74.0% overall accuracy for raw images compared to a substantial  $85.8 \pm 4.9\%$  overall accuracy for virtual images). As a result, we conclusively establish that the application of SymAE redatuming proves beneficial when undertaking land-cover discrimination tasks.

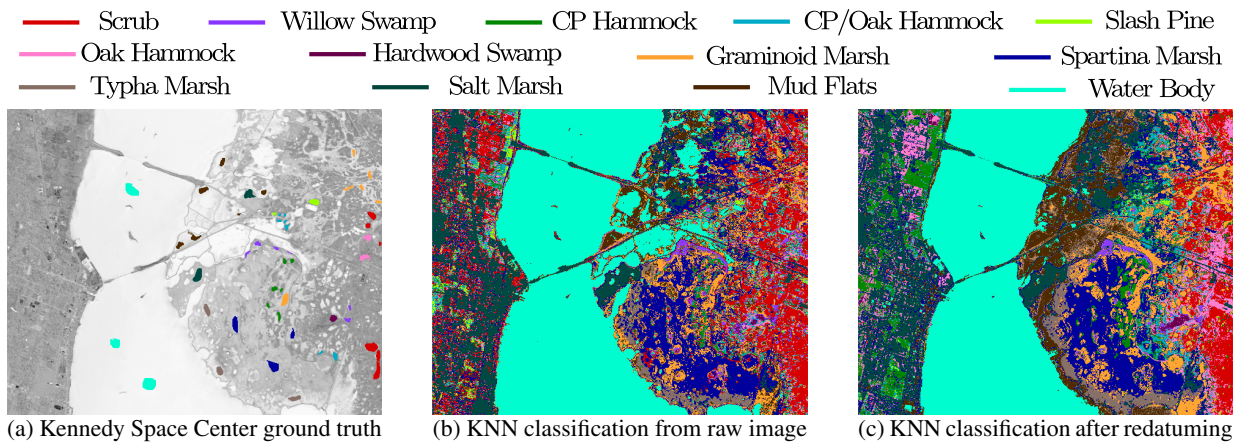


Figure 5: K-Nearest Neighbors (KNN) pixel classification results on KSC scene maps. (a) ground truth map of the KSC scene, serving as the baseline. (b) Pixel classification utilizing KNN on the raw image, resulting in an overall accuracy of 81.6% for the test set ground truth. (c) Pixel classification conducted on a virtual image with uniformized nuisance, demonstrating an elevated average overall accuracy of 92.8%. Virtual images, generated through the redatuming process, contribute to enhanced pixel classification accuracy, highlighting their valuable role in advancing hyperspectral image analysis.

While more complex models, such as the Random Forests and KNN, exhibit relatively consistent performance, the substantial variance in accuracy when employing a linear SVM on different virtual images highlights the decisive role of reference pixel selection in shaping classification outcomes. This influence is not uniform across all cases, with some reference pixels leading to remarkable enhancements while others, albeit rarely, induce performance deterioration. On average, our results demonstrate a significant overall improvement in classification performance. Nonetheless, the selection of an appropriate reference pixel can pose challenges. In subsequent sections, we introduce an alternative method for leveraging SymAE to further enhance clustering and classification.

### 4.3 Surface-Reflectance Code: Clustering Analysis

The alternative method we mentioned is leveraging reflectance code generated by REnc for clustering and classification tasks. In addition to generating virtual images, a trained SymAE also provides us with a reflectance code, denoted as  $\text{REnc}_1(D[\cdot])$ , for each pixel. Since this code is intended to remain unaffected by atmospheric distortions and other forms of nuisance variability, the focus of this section is to leverage this code for clustering analysis. Our objective is to investigate whether the reflectance latent space can effectively disentangle classes characterized by subtle differences in reflectivity, such as neighboring vegetation types.

In the case of KSC experiment, we initially sampled 100 pixels from two ground truth classes, Slash Pine and Oak Hammock (Figure 6a). We performed Principal Component Analysis (PCA) on their spectra and observed that they closely overlapped in the first two principal components, making their separation challenging (Figure 6b). Expanding the number of components did not significantly alter the results. Subsequently, we explored an alternative approach by clustering the pixels based on the reflectance code. The 2-D linear subspace of the reflectance code is depicted in Figure 6c.

To quantitatively assess this improvement, we applied the K-means clustering algorithm to both the raw spectra space and the reflectance code latent space. We repeated this process 100 times with randomly sampled pixels from the classes. The results indicated that, on average, K-means clustering in the raw spectra space achieved an accuracy of 75.5%, while in the latent reflectance code space, it achieved 95.9%. This represents a substantial improvement of 20.4% in percentage accuracy. Even more challenging were the classes CP Hammock and CP/Oak Hammock

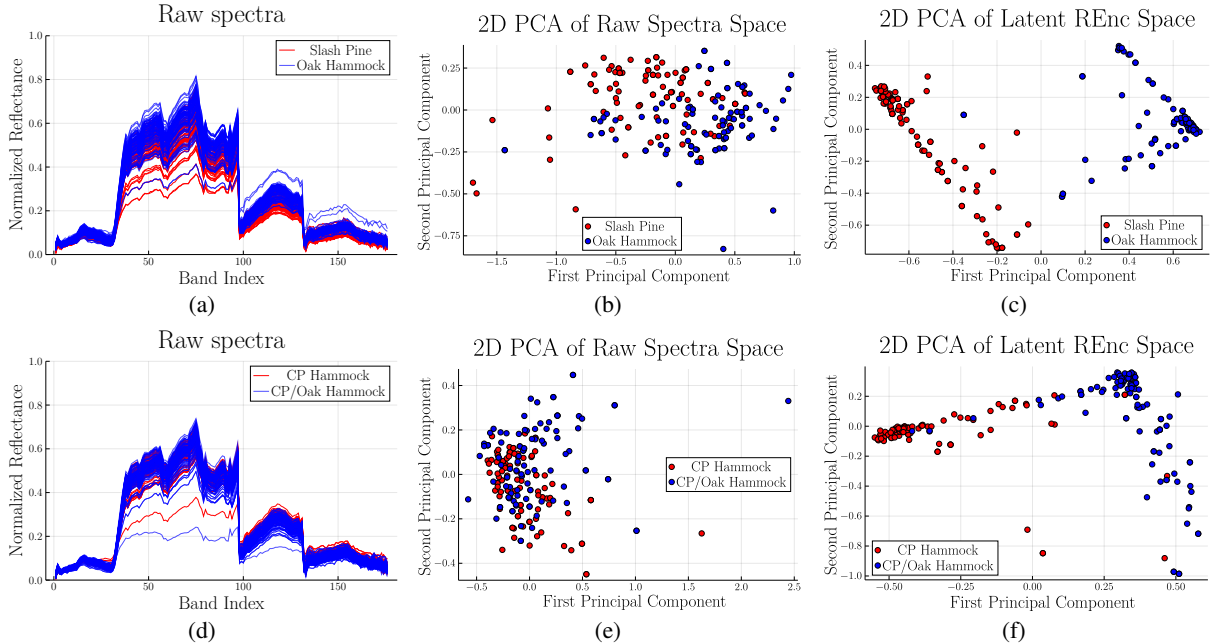


Figure 6: SymAE allows for clustering pixels based on reflectance code, i.e.,  $\text{REnc}_1(D[\cdot])$  that is not affected by the atmospheric variations and other nuisance effects. (a,d) Raw spectra of spectrally close-by classes. (b,e) These classes are hard to separate in 2D raw spectra space. (c,f) Notice that the classes that otherwise have subtle differences in raw spectra are much easier to discriminate in latent coherent code space. Most significant improvement in the K-means clustering experiment we described is observed in classes with subtle differences like CP Hammock and CP/Oak Hammock depicted in (d),(e) and (f).

(Figure 6d, 6e), which exhibited even closer proximity. In raw spectra space, the average clustering accuracy was 53.3%. In contrast, when we performed clustering in the REnc space, we obtained an accuracy of 89.9%, reflecting a notable improvement of 36.6%.

In our comprehensive pairwise clustering experiment encompassing all ground truth classes within the scene, we observed an average improvement of 12.0% in classification accuracy across all class pairs. Notably, the most substantial improvements were evident among classes characterized by subtle differences. These pairwise enhancements are graphically illustrated in Figure 7. These findings underscore the substantial effectiveness of REnc in capturing class-specific features essential for distinguishing between closely related classes.

1	0.0	11.9	45.8	41.1	22.6	37.7	39.9	2.4	6.9	4.7	4.6	0.4	0.2
2	11.9	0.0	12.2	15.9	21.7	11.9	5.9	19.6	32.4	20.9	5.2	3.3	0.4
3	45.8	12.2	0.0	36.3	23.2	42.2	44.6	0.9	2.8	3.9	3.6	0.2	0.0
4	41.1	15.9	36.3	0.0	14.9	32.2	45.1	0.6	3.8	4.5	4.4	0.5	0.7
5	22.6	21.7	23.2	14.9	0.0	20.4	28.0	1.9	3.3	5.4	3.6	0.4	0.0
6	37.7	11.9	42.2	32.2	20.4	0.0	34.3	1.1	4.9	2.7	1.0	0.1	0.0
7	39.9	5.9	44.6	45.1	28.0	34.3	0.0	1.3	1.3	2.6	1.3	0.0	0.0
8	2.4	19.6	0.9	0.6	1.9	1.1	1.3	0.0	21.3	46.0	4.7	24.2	11.7
9	6.9	32.4	2.8	3.8	3.3	4.9	1.3	21.3	0.0	17.5	6.5	2.3	0.0
10	4.7	20.9	3.9	4.5	5.4	2.7	2.6	46.0	17.5	0.0	5.2	22.3	7.9
11	4.6	5.2	3.6	4.4	3.6	1.0	1.3	4.7	6.5	5.2	0.0	2.4	1.9
12	0.4	3.3	0.2	0.5	0.4	0.1	0.0	24.2	2.3	22.3	2.4	0.0	16.0
13	0.2	0.4	0.0	0.7	0.0	0.0	0.0	11.7	0.0	7.9	1.9	16.0	0.0
	1	2	3	4	5	6	7	8	9	10	11	12	13

Figure 7: Heatmap illustrating improvement in clustering in KSC dataset. The matrix elements indicate the percentage accuracy difference between K-means clustering in the latent reflectance code,  $\text{REnc}_1(D[\cdot])$ , and clustering in the raw spectral data while doing pairwise unsupervised clustering between land-cover classes. The numbers on axes indicate the class indices, following same ordering as in 1. This heatmap pertains to the ground truth-based training scenario and the clustering was done on test set. Pairs that show minimal improvement are those that already exhibit significant separation in raw spectra.

#### 4.4 Using Surface-Reflectance Code: Classification

Building on the insights gained from the previous section, we now turn our focus to the application of SymAE for hyperspectral image (HSI) classification, utilizing the reflectance encoder REnc to extract class-specific information. We trained a feed-forward dense layer neural network to predict the ground truth class label based on a given pixel’s reflectance code. The classification was performed on a pixel-by-pixel basis, resulting in an overall test accuracy of 94.65%. To the best of our knowledge, this represents the highest classification accuracy achieved using solely spectral information, without leveraging spatial correlation within the scene for this train-test split ratio. The classification results are detailed in Table 2.

In our pursuit of comparing SymAE with leading HSI classification methods that adopt a combined spatial-spectral approach, we sought to incorporate spatial information into our experiments. Our approach involved assigning labels to each pixel based on the mode of labels obtained from its spectral feed-forward network and its eight adjacent neighbors. This process was iterated three times, effectively applying a form of spatial smoothing. The results of this approach are presented in Table 2, showcasing an overall accuracy of 99.48%. This performance closely aligns with state-of-the-art methods such as SSRPnet [27] and CVSSN [28], which harness spatial information more comprehensively.

Furthermore, we extended our assessment to include two widely used HSI datasets: Indian Pines and Pavia University. Employing the same number of training samples as Hong et al. did when introducing SpectralFormer [29], the current state-of-the-art backbone network for extracting spectral features in HSI classification, our results on both datasets demonstrated superior classification performance compared to SpectralFormer when using purely spectral features, numerical results of which are demonstrated in Table 5.

Table 2: Classification of test pixels from Kennedy Space Center dataset using SymAE generated reflectance code.

No.	Class	Training Samples	Test Samples	Pixel-based Classification Accuracy	Classification Accuracy After Spatial Smoothing
1	Scrub	77	684	95.61 %	97.71 %
2	Willow Swamp	25	218	96.79 %	100.0 %
3	CP Hammock	26	230	85.22 %	98.26 %
4	CP/Oak Hammock	26	226	80.53 %	96.02 %
5	Slash Pine	17	144	77.08 %	94.44 %
6	Oak Hammock	23	206	77.67 %	100.0 %
7	Hardwood Swamp	11	94	88.23 %	100.0 %
8	Graminoid Marsh	44	387	96.90 %	100.0 %
9	Spartina Marsh	52	468	97.44 %	100.0 %
10	Typha Marsh	38	366	97.27 %	100.0 %
11	Salt Marsh	42	377	98.14 %	99.73 %
12	Mud Flats	47	456	98.90 %	100.0 %
13	Water Body	91	836	100.0 %	100.0 %
	Overall Accuracy			94.65 %	99.48 %
	Average Accuracy			91.53 %	99.09 %
	Kappa $\times 100$			94.04	99.43

Table 3: Classification of test pixels from Pavia University dataset using SymAE generated reflectance code.

No.	Class	Training Samples	Test Samples	Pixel-based Classification Accuracy	Classification Accuracy After Spatial Smoothing
1	Asphalt	548	6083	93.65 %	97.63 %
2	Meadows	540	18109	93.81 %	97.91 %
3	Gravel	392	1707	83.42 %	91.86 %
4	Trees	524	2520	98.58 %	99.37 %
5	Painted metal sheets	265	1080	100.0 %	100.0 %
6	Bare soil	532	4497	97.89 %	100.0 %
7	Bitumen	375	955	91.62 %	95.39 %
8	Self blocking bricks	514	3168	88.35 %	97.03 %
9	Shadows	94	716	100.0 %	100.0 %
	Overall Accuracy			93.90 %	97.90 %
	Average Accuracy			94.15 %	97.69 %
	Kappa $\times 100$			91.76	97.14

Table 4: Classification of test pixels from Indian Pines dataset using SymAE generated reflectance code.

No.	Class	Training Samples	Test Samples	Pixel-based Classification Accuracy	Classification Accuracy After Spatial Smoothing
1	Alfalfa	15	31	96.77 %	100.0 %
2	Corn-notill	50	1378	74.02 %	82.80 %
3	Corn-mintill	50	780	76.28 %	88.72 %
4	Corn	50	187	81.82 %	99.47 %
5	Grass-pasture	50	433	95.38 %	97.69 %
6	Grass-trees	50	680	91.18 %	97.50 %
7	Grass-pasture-mowed	15	13	100.0 %	92.31 %
8	Hay-windrowed	50	428	98.36 %	99.53 %
9	Oats	15	5	100.0 %	80.00 %
10	Soybean-no-till	50	922	82.65 %	95.77 %
11	Soybean-min-till	50	2405	69.90 %	87.69 %
12	Soybean-clean	50	543	85.82 %	98.16 %
13	Wheat	50	155	99.35 %	99.35 %
14	Woods	50	1215	88.48 %	95.97 %
15	Buildings-Grass-Trees-Drives	50	336	80.65 %	95.54 %
16	Stone-Steel-Towers	50	43	100.0 %	100.0 %
	Overall Accuracy			80.82 %	91.97 %
	Average Accuracy			88.79 %	94.41 %
	Kappa $\times 100$			78.19	90.82

Table 5: Comparison between classification accuracies of SymAE and SpectralFormer using only spectral information.

HSI Scene	Metric	SpectralFormer	SymAE
Pavia University	Overall Accuracy	87.94 %	<b>93.90 %</b>
	Average Accuracy	87.47 %	<b>94.15 %</b>
	Kappa $\times 100$	83.58	<b>91.76</b>
Indian Pines	Overall Accuracy	78.55 %	<b>80.82 %</b>
	Average Accuracy	84.68 %	<b>88.79 %</b>
	Kappa $\times 100$	75.54	<b>78.19</b>

This notable improvement in performance emphasizes SymAE’s strong proficiency in spectral feature extraction. As Sun et al. pointed out in their study [30], spectral features play a fundamental role in accurately characterizing the distribution of ground objects, serving as crucial discriminative factors in HSIs. Despite these promising results, it is important to note that purely spectral methods are susceptible to scattered noise, which can lead to lower accuracy levels. Even after applying spatial smoothing, our accuracies on these datasets did not match the leading spectral-spatial methods. These findings collectively underscore SymAE’s potential for hyperspectral image classification and motivate further exploration into advanced techniques for incorporating spatial information. Such exploration holds the promise of yielding even greater classification performance.

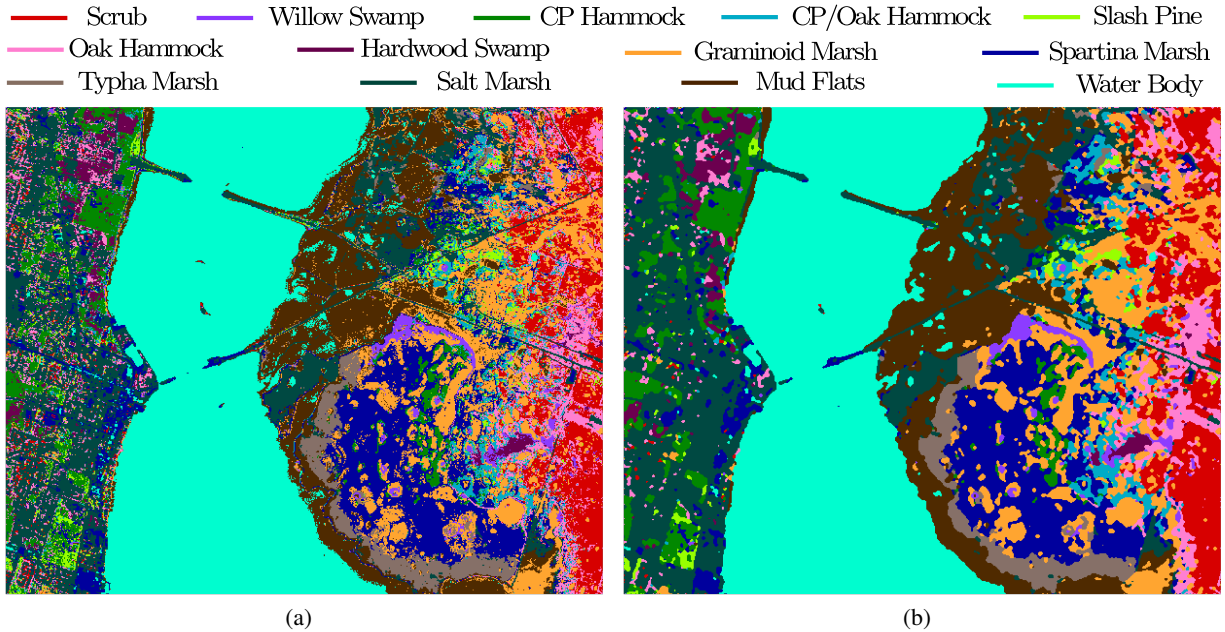


Figure 8: Classification of SymAE-generated reflectance code for the Kennedy Space Center scene. a) Pixels are labeled using purely spectral information. b) Spatial smoothing applied to (a) which improved the classification accuracy.

## 5 Training SymAE Without Ground Truth

Many remote sensing datasets lack ground truth labels for different spectra, making it challenging to group spectra before SymAE training. In such scenarios, we rely on the assumption of spatial correlation in the reflectance information, enabling us to group pixels located nearby within the scene. This assumption implies that spatially neighboring pixels likely belong to the same class. This approach, which assumes that spatial proximity implies class similarity, provides structural organization to the data even when explicit labels are absent, costly to obtain, or difficult to acquire. This conjecture is particularly valid when dealing with datasets characterized by significant spatial correlation, as seen in examples like the Indian Pines dataset, which contains nearly 10 classes (farmlands) with extensive spatial coverage.



Guided by this premise, we partitioned the KSC scene into small  $3 \times 3$  pixel groups for SymAE training. Our experiments on the KSC dataset revealed an average enhancement of 8.7% in pairwise K-means clustering accuracy, akin to the results discussed in subsection 4.3, when utilizing the reflectance code instead of raw spectra. It is crucial to note that we did not observe this improvement when spectra were randomly grouped within the scene. As expected, random spectral grouping led to significantly poorer clustering performance.

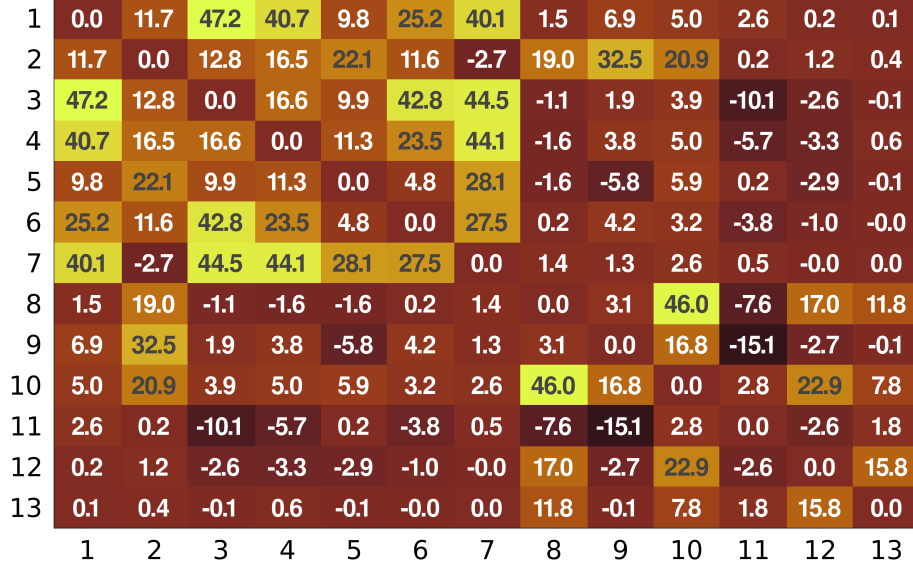


Figure 9: Heatmap illustrating the improvement in K-means clustering achieved by utilizing the latent reflectance code in place of raw spectra, similar to Figure 7, but without relying on ground truth labels. The heatmap highlights substantial performance enhancements across most classes, while also indicating instances of performance decline among specific class pairs.

The clustering analysis, as illustrated in Figure 9, provides valuable insights into the performance of SymAE concerning pair-wise classes. We expect that the pixels situated close to class boundaries might not be well represented in SymAE’s latent space due to the simplicity of the grouping approach employed. As evident, the performance of SymAE does exhibit variations across different classes. In fact, there is evidence of performance degradation for certain classes when compared to the use of raw spectra — most of these classes are not spatially contiguous or have a small extent.

This observation motivated us to verify this unsupervised approach further, in a more concentrated setting. We chose a small patch of land on the Indian Pines data set where our spatial-proximity assumption would seem to fit well. The patch primarily contains two close-by classes: Soybean-clean and Corn-min-till. The patch and the clustering analysis of the pixels are depicted in Figure 10. In line with our prior observations from subsection 4.3, the initial representation of raw spectral data using the first two principal components does not reveal clear class separations. However, a substantial enhancement in structure becomes evident when examining the latent reflectance code space, where class distinctions become considerably more discernible. It is worth highlighting that pixels positioned near or along the class boundaries present a challenge in terms of differentiation. This observation aligns with our underlying assumption of spatial proximity, which groups border-adjacent pixels together prior to the SymAE training process, even if they genuinely belong to distinct classes. On a positive note, pixels situated at a greater distance from the class boundaries, or beyond their immediate vicinity, exhibit a distinct separation within the latent space. This facilitates their effective classification using a straightforward decision boundary. The results illustrate improved clustering within the latent space. This unsupervised grouping approach holds potential utility in settings where ground truth information is unavailable, such as remote or extraterrestrial environments. In future research endeavors, we will focus on developing advanced and robust methodologies for prior grouping, especially in unsupervised contexts.

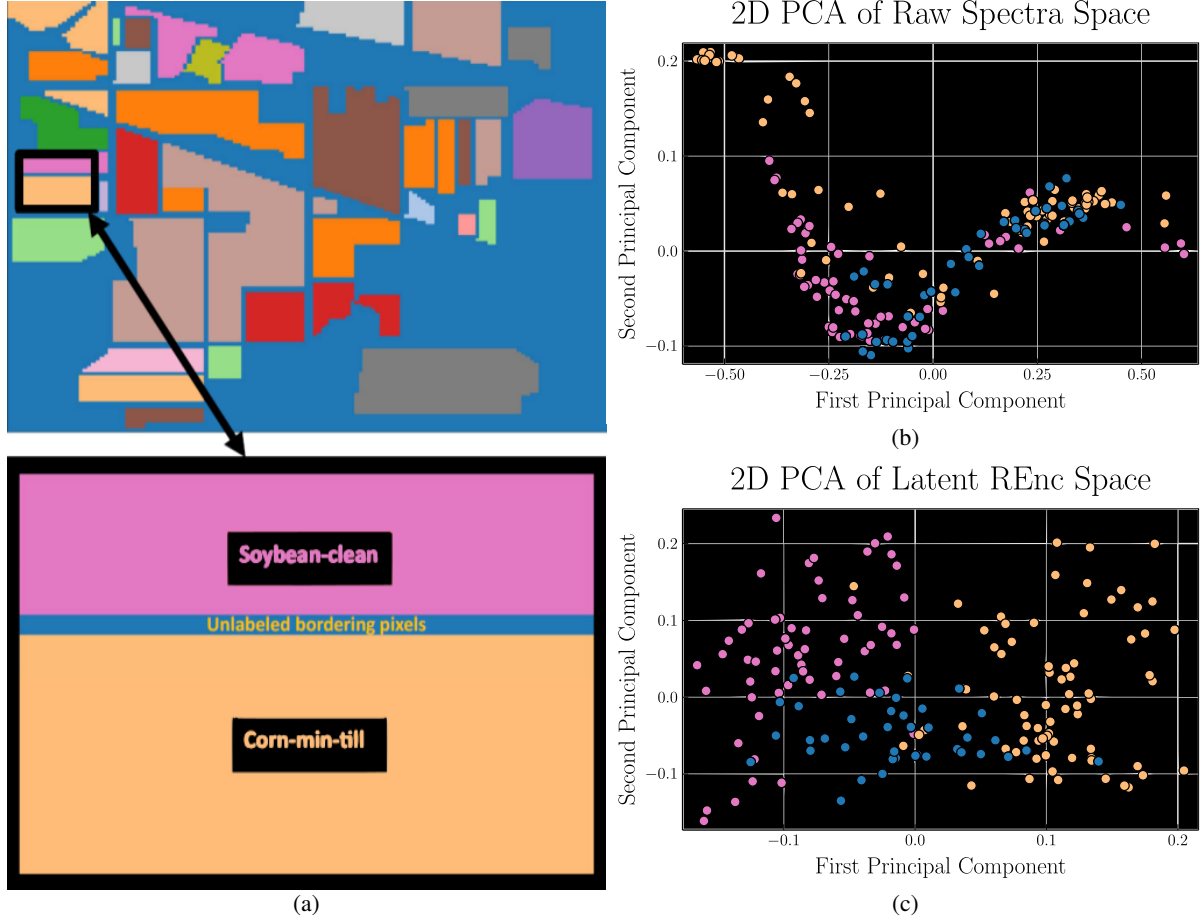


Figure 10: A focused testing of SymAE without ground truth in Indian Pines scene. (a) A selected sub-region within the scene characterized by favorable spatial conditions to test SymAE without ground truth. (b) A 2D representation of the raw spectral space, utilizing the same color scheme as in (a) to visualize data points. (c) The 2D latent space of the reflectance code. Pixels near class boundaries pose challenges for differentiation, aligning with our spatial proximity assumption that groups border-adjacent pixels together. However, pixels farther from class boundaries exhibit clear separation within this space, aiding straightforward discrimination.

## 6 Discussion

In this section, we delve into the distinctive training phenomena observed during SymAE training, consider potential implications and applications of this architecture, and outline areas with room for future improvements.

### 6.1 Atypical training nature of SymAE and choice of activation function

We observed an intriguing phenomenon during the training process of SymAE. Initially, the training loss curve exhibits a declining trend, followed by a subsequent increase in loss, and then eventually reaching a state of saturation. Notably, this increase in loss corresponds with an improvement in K-means clustering performance within the latent space. We conjecture that this phenomenon is attributable to the feature transfer dynamics between the encoding modules, specifically from NEnc to REnc, and the attention of decoder Fuse to them. In the early stages of SymAE training, NEnc inadvertently captures coherent reflectance features. As training progresses, dropout layers intermittently obfuscate these features. Consequently, Fuse works to extract information from REnc, which continually supplies data. Over time, Fuse adjusts to make the most of REnc-sourced data. However, it is important to note that due to REnc’s inherent constraints, the quality of reconstruction falls short of what an unconstrained dense layer network can achieve. This discrepancy leads to the observed increase in loss during training.



## Atypical Loss Curves

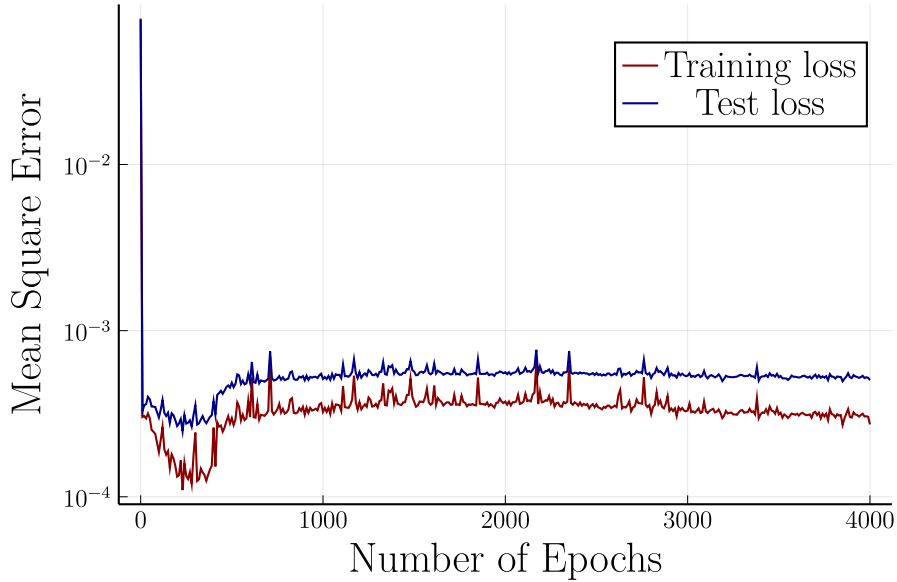


Figure 11: Atypical training curves we encountered while training SymAE. At the outset, the training loss curve shows a descending trend, which is subsequently followed by a rise in loss, ultimately reaching a state of saturation.

Having a sufficiently long nuisance code length can mitigate this atypical behavior, but that would significantly increase the number of training updates required to achieve effective disentanglement of nuisance and reflectance features in latent space. Empirically, we consistently achieved satisfactory performance of SymAE upon 3000 to 4000 training epochs with 2048 minibatches, each minibatch containing 256 datapoints in our experiments.

We would also like to highlight our selection of the Leaky ReLU with slope parameter 0.5 as activation function. Our decision in this regard was guided by empirical observations from our study. Throughout our investigations, we observed that traditional activation functions, including tanh and ReLU, exhibited susceptibility to vanishing gradient issues and the *dying ReLU* problem [31]. These challenges are particularly pronounced in SymAE, given its inherent stochastic nature. Our experimental results unequivocally demonstrated that the Leaky ReLU, characterized by its inherent flexibility, effectively mitigates these issues, thus establishing itself as the better choice for our network.

### 6.2 Applications and future possibilities with SymAE

Symmetric Autoencoder (SymAE) introduces a data-driven architecture with significant potential applications in challenging scenarios where physical modeling is impractical. For instance, it can find utility in remote sensing tasks conducted in extraterrestrial environments or locations with limited information available about nuisance factors. SymAE offers an alternative approach that sidesteps the complexity associated with developing intricate physical models.

Some key implications and potential future applications of SymAE encompass:

- **Atmospheric Correction Alternative and Data Quality Enhancement:** SymAE’s capacity to disentangle surface reflectance information from nuisances like atmospheric interference and sensor noise provides an appealing alternative to conventional atmospheric correction methods. This has the potential to significantly enhance data quality, particularly in settings where physical modeling is unfeasible.
- **Scenario Exploration and Virtual Imaging:** SymAE’s ability to generate virtual images under diverse conditions facilitates scenario exploration and hypothesis testing, supporting more informed decision-making.
- **Data Augmentation and Model Training:** SymAE’s capability to generate synthetic data could bolster machine learning model training, enhancing model robustness. This could prove particularly valuable in data-scarce scenarios.

- **Enhanced Hyperspectral Signature Analysis:** SymAE’s capacity to reduce intra-class variance enhances hyperspectral signature analysis, potentially aiding in finer material differentiation and environmental change detection.
- **Spatial-Spectral Fusion:** Future investigations can delve into the integration of spatial information with spectral data, further extending SymAE’s utility in applications such as classification and clustering.

### 6.3 Scope for improvement

While SymAE has shown promising results, there are certain aspects that warrant further improvement. One significant consideration is the time required to achieve effective disentanglement between reflectance and nuisance features. During our experiments, we observed that the inherent stochastic nature of SymAE training demanded a substantial investment of approximately 12 hours to reach a point where reflectance and nuisance features were satisfactorily disentangled, based on the configurations chosen for the datasets in this study. This extended training duration prompts the exploration of more efficient training strategies and architectural refinements, offering a compelling avenue for future research. Another area of improvement relates to the initial grouping method employed in the fully unsupervised scenario presented here. This method, while effective to some extent, is relatively simplistic and susceptible to misclassifying pixels from distinct classes as a single group. In future investigations, we aim to enhance this grouping algorithm to minimize the probability of erroneously assigning pixels from different classes to the same group. This refinement will contribute to the overall robustness of the SymAE approach, particularly in scenarios where ground truth labels are unavailable or challenging to obtain.

## 7 Conclusion

In conclusion, this study has introduced the Symmetric Autoencoder (SymAE) architecture in the context of Hyperspectral Imaging (HSI) analysis and demonstrated its capabilities. SymAE’s unique approach to disentangling nuisance features from surface reflectance features in a purely data-driven manner presents potential opportunities for advancing HSI data preprocessing and analysis. We have showcased the practicality of SymAE by utilizing it to generate virtual images through reformatting spectra, effectively uniformizing nuisance effects across hyperspectral image spectra and reducing intra-class variance. Compared to denoising autoencoders, SymAE offers superior performance in this regard. Furthermore, the use of virtual images enhances various image analysis tasks, which were particularly demonstrated in classification and clustering. Our work has also highlighted the extraction of reflectance codes, which remain independent of nuisance effects. We demonstrated the capability of SymAE to extract spectral features, enhancing clustering and classification performance, outperforming state-of-the-art architectures in the process. To enhance accuracy further, we introduced a spatial smoothing technique, complementing SymAE’s spectral capabilities. While this narrows the performance gap between our purely spectral approach with state-of-the-art spectral-spatial classification methods, realizing the full potential of spatial information in classification requires more advanced methodologies. Additionally, we proposed a method for applying SymAE without relying on ground truth information, opening possibilities for extraterrestrial settings or environments where modeling nuisance phenomena is challenging. However, the current grouping method before SymAE training without ground truth requires refinement, offering an avenue for future research. Our architecture has the potential to find applications in various domains, including spectral signature analysis, data augmentation, and scenario analysis, making Symmetric Autoencoders a tool with promise in HSI analysis, inviting further exploration and evaluation within the research community.

## 8 Acknowledgements

All experimental procedures were conducted using the Julia programming language on a local computing system equipped with 128 GB RAM, an AMD Ryzen Threadripper 3960X 24-core processor, and a 24 GB NVIDIA GeForce RTX 3090 GPU. We would also like to acknowledge the use of ChatGPT, an AI language model developed by OpenAI, which played a significant role in refining portions of the text in this paper. The contributions of ChatGPT were valuable in enhancing the clarity and coherence of our writing.

## References

- [1] José M Bioucas-Dias, Antonio Plaza, Gustavo Camps-Valls, Paul Scheunders, Nasser Nasrabadi, and Jocelyn Chanussot, “Hyperspectral remote sensing data analysis and future challenges,” *IEEE Geoscience and remote sensing magazine*, vol. 1, no. 2, pp. 6–36, 2013.
- [2] Gary A Shaw and Hsiaohua K Burke, “Spectral imaging for remote sensing,” *Lincoln laboratory journal*, vol. 14, no. 1, pp. 3–28, 2003.
- [3] Mark A. Kramer, “Nonlinear principal component analysis using autoassociative neural networks,” *AIChE Journal*, vol. 37, no. 2, pp. 233–243, 1991.
- [4] I Goodfellow, Y Bengio, and A Courville, *Deep learning*, MIT Press, 2016.
- [5] Pawan Bharadwaj, Matthew Li, and Laurent Demanet, “Redatuming physical systems using symmetric autoencoders,” 2022.
- [6] Bo-Cai Gao, Kathleen B. Heidebrecht, and Alexander F.H. Goetz, “Derivation of scaled surface reflectances from aviris data,” *Remote Sensing of Environment*, vol. 44, no. 2, pp. 165–178, 1993, Airbone Imaging Spectrometry.
- [7] Bo-Cai Gao and Curtiss O. Davis, “Development of a line-by-line-based atmosphere removal algorithm for airborne and spaceborne imaging spectrometers,” in *Imaging Spectrometry III*, Michael R. Descour and Sylvia S. Shen, Eds. International Society for Optics and Photonics, 1997, vol. 3118, pp. 132 – 141, SPIE.
- [8] Minzheng Duan, Qilong Min, and Daren Lü, “A polarized radiative transfer model based on successive order of scattering,” *Advances in Atmospheric Sciences*, vol. 27, pp. 891–900, 2010.
- [9] Bo Cai Gao, Marcos J. Montes, Curtiss O. Davis, and Alexander F.H. Goetz, “Atmospheric correction algorithms for hyperspectral remote sensing data of land and ocean,” *Remote Sensing of Environment*, vol. 113, 9 2009.
- [10] Nisha Rani, Venkata Ravibabu Mandla, and Tejpal Singh, “Evaluation of atmospheric corrections on hyperspectral data with special reference to mineral mapping,” *Geoscience Frontiers*, vol. 8, pp. 797–808, 7 2017.
- [11] DA Roberts, Y Yamaguchi, and RJP Lyon, “Comparison of various techniques for calibration of ais data,” *NASA STI/Recon Technical Report N*, vol. 87, pp. 21–30, 1986.
- [12] James E Conel, Robert O Green, Gregg Vane, Carol J Bruegge, Ronald E Alley, and Brian J Curtiss, “Ais-2 radiometry and a comparison of methods for the recovery of ground reflectance,” in *Proceedings of the 3rd airborne imaging spectrometer data analysis workshop*, 1987.
- [13] Lei Ma, Yu Liu, Xueliang Zhang, Yuanxin Ye, Gaofei Yin, and Brian Alan Johnson, “Deep learning in remote sensing applications: A meta-analysis and review,” *ISPRS journal of photogrammetry and remote sensing*, vol. 152, pp. 166–177, 2019.
- [14] Fangcao Xu, Guido Cervone, Gabriele Franch, and Mark Salvador, “Multiple geometry atmospheric correction for image spectroscopy using deep learning,” *Journal of Applied Remote Sensing*, vol. 14, pp. 1, 6 2020.
- [15] Jian Sun, Fangcao Xu, Guido Cervone, Melissa Gervais, Christelle Wauthier, and Mark Salvador, “Automatic atmospheric correction for shortwave hyperspectral remote sensing data using a time-dependent deep neural network,” *ISPRS Journal of Photogrammetry and Remote Sensing*, vol. 174, pp. 117–131, Apr. 2021.
- [16] Diego Valsesia and Enrico Magli, “Permutation invariance and uncertainty in multitemporal image super-resolution,” *IEEE Transactions on Geoscience and Remote Sensing*, vol. 60, pp. 1–12, 2021.
- [17] Ian Goodfellow, Jean Pouget-Abadie, Mehdi Mirza, Bing Xu, David Warde-Farley, Sherjil Ozair, Aaron Courville, and Yoshua Bengio, “Generative adversarial networks,” *Communications of the ACM*, vol. 63, no. 11, pp. 139–144, 2020.
- [18] Lin Zhu, Yushi Chen, Pedram Ghamisi, and Jón Atli Benediktsson, “Generative adversarial networks for hyperspectral image classification,” *IEEE Transactions on Geoscience and Remote Sensing*, vol. 56, no. 9, pp. 5046–5063, 2018.
- [19] Carl Doersch, “Tutorial on variational autoencoders,” *arXiv preprint arXiv:1606.05908*, 2016.
- [20] Manzil Zaheer, Satwik Kottur, Siamak Ravanbakhsh, Barnabás Póczos, Ruslan Salakhutdinov, and Alexander J. Smola, “Deep sets,” *Advances in Neural Information Processing Systems*, , no. ii, pp. 3392–3402, apr 2017.
- [21] Nitish Srivastava, Geoffrey Hinton, Alex Krizhevsky, Ilya Sutskever, and Ruslan Salakhutdinov, “Dropout: a simple way to prevent neural networks from overfitting,” *The journal of machine learning research*, vol. 15, no. 1, pp. 1929–1958, 2014.

- [22] Steven M Adler-Golden, Michael W Matthew, Lawrence S Bernstein, Robert Y Levine, Alexander Berk, Steven C Richtsmeier, Prabhat K Acharya, Gail P Anderson, Jerry W Felde, JA Gardner, et al., “Atmospheric correction for shortwave spectral imagery based on modtran4,” in *Imaging Spectrometry V*. International Society for Optics and Photonics, 1999, vol. 3753, pp. 61–69.
- [23] Joseph W Boardman, “Post-atrem polishing of aviris apparent reflectance data using effort: a lesson in accuracy versus precision,” in *Summaries of the seventh JPL airborne earth science workshop*, 1998, vol. 1, p. 53.
- [24] Michael Innes, Elliot Saba, Keno Fischer, Dhairya Gandhi, Marco Concetto Rudilosso, Neethu Mariya Joy, Tejan Karmali, Avik Pal, and Viral Shah, “Fashionable modelling with flux,” *CoRR*, vol. abs/1811.01457, 2018.
- [25] Pascal Vincent, Hugo Larochelle, Yoshua Bengio, and Pierre-Antoine Manzagol, “Extracting and composing robust features with denoising autoencoders,” in *Proceedings of the 25th international conference on Machine learning*, 2008, pp. 1096–1103.
- [26] Chen Xing, Li Ma, Xiaoquan Yang, et al., “Stacked denoise autoencoder based feature extraction and classification for hyperspectral images,” *Journal of Sensors*, vol. 2016, 2016.
- [27] Chunbo Cheng, Hong Li, Jiangtao Peng, Wenjing Cui, and Liming Zhang, “Hyperspectral image classification via spectral-spatial random patches network,” *IEEE Journal of Selected Topics in Applied Earth Observations and Remote Sensing*, vol. 14, pp. 4753–4764, 2021.
- [28] Mingsong Li, Yikun Liu, Guangkuo Xue, Yuwen Huang, and Gongping Yang, “Exploring the relationship between center and neighborhoods: Central vector oriented self-similarity network for hyperspectral image classification,” *IEEE Transactions on Circuits and Systems for Video Technology*, vol. 33, no. 4, pp. 1979–1993, 2022.
- [29] Danfeng Hong, Zhu Han, Jing Yao, Lianru Gao, Bing Zhang, Antonio Plaza, and Jocelyn Chanussot, “Spectralformer: Rethinking hyperspectral image classification with transformers,” *IEEE Transactions on Geoscience and Remote Sensing*, vol. 60, pp. 1–15, 2021.
- [30] Yifan Sun, Bing Liu, Xuchu Yu, Anzhu Yu, Pengqiang Zhang, and Zhixiang Xue, “Exploiting discriminative advantage of spectrum for hyperspectral image classification: Spectralformer enhanced by spectrum motion feature,” *IEEE Geoscience and Remote Sensing Letters*, vol. 20, pp. 1–5, 2022.
- [31] Lu Lu, Yeonjong Shin, Yanhui Su, and George Em Karniadakis, “Dying relu and initialization: Theory and numerical examples,” *arXiv preprint arXiv:1903.06733*, 2019.